Impact of Stratiform Rainband Heating on the Tropical Cyclone Wind Field in Idealized Simulations

CHAU-LAM YU AND ANTHONY C. DIDLAKE, JR.

Department of Meteorology and Atmospheric Science, The Pennsylvania State University, University Park, Pennsylvania

(Manuscript received 12 November 2018, in final form 28 May 2019)

ABSTRACT

Using idealized simulations, we examine the storm-scale wind field response of a dry, hurricane-like vortex to prescribed stratiform heating profiles that mimic tropical cyclone (TC) spiral rainbands. These profiles were stationary with respect to the storm center to represent the diabatic forcing imposed by a quasi-stationary rainband complex. The first profile was typical of stratiform precipitation with heating above and cooling below the melting level. The vortex response included a mesoscale descending inflow and a midlevel tangential jet, consistent with previous studies. An additional response was an inward-spiraling low-level updraft radially inside the rainband heating. The second profile was a modified stratiform heating structure derived from observations and consisted of a diagonal dipole of heating and cooling. The same features were found with stronger magnitudes and larger vertical extents. The dynamics and implications of the forced low-level updraft were examined. This updraft was driven by buoyancy advection because of the stratiform-induced low-level cold pool. The stationary nature of the rainband diabatic forcing played an important role in modulating the required temperature and pressure anomalies to sustain this updraft. Simulations with moisture and full microphysics confirmed that this low-level updraft response was robust and capable of triggering sustained deep convection that could further impact the storm evolution, including having a potential role in secondary eyewall formation.

1. Introduction

Spiral rainbands are banded precipitation features that populate the region outside of a tropical cyclone (TC) eyewall, forming a spiral or circular arc of clouds and precipitation observed in radar and satellite images (Willoughby et al. 1984; Houze 2010; Hence and Houze 2012). As prominent features in the larger storm, rainbands can have a significant impact on the intensity, size, and structure of an evolving TC. Under the influence of environmental wind shear, rainbands often form an organized complex that remains quasi stationary with respect to the TC center, and thus is termed a "stationary band complex" (SBC; Willoughby et al. 1984). In the upwind portion of the SBC, new convection is triggered, forming discrete convective cells or a connected band (Barnes et al. 1983; Powell 1990; May 1996). These active convective cells are noted to be associated with clear overturning circulations and convective-scale tangential wind jets, where the depth of the jet and reflectivity tower largely depends on distance from the storm center (Didlake and Houze 2013a). Traveling along the rainband, convection matures and collapses, while slowly falling ice particles originating from the active convection upwind are advected even farther downwind. In these downwind portions of the rainband complex, ice particles fall out to form a broad, homogeneous precipitation band that predominantly displays stratiform characteristics (May and Holland 1999; Hence and Houze 2008, 2012; Didlake and Houze 2013b, hereafter DH13; Didlake and Kumjian 2017).

Owing to its large spatial coverage and close proximity to the eyewall, the stratiform rainband likely plays an important role in the dynamical and structural evolution of TCs, especially for secondary eyewall formation (e.g., Tyner et al. 2018; Didlake et al. 2018). To better understand the dynamical role of rainbands, Moon and Nolan (2010, hereafter MN10) used idealized simulations to study the storm-scale wind field response of a hurricane-like vortex to idealized convective and

Supplemental information related to this paper is available at the Journals Online website: https://doi.org/10.1175/JAS-D-18-0335.s1.

Corresponding author: Chau Lam Yu, cuy89@psu.edu

DOI: 10.1175/JAS-D-18-0335.1

stratiform heating patterns rotating around the hurricane inner core. Their stratiform heating experiments used a typical, idealized heating structure for convection-generated stratiform precipitation, having latent heating above and latent cooling below the melting level to match the water phase changes at these levels. The vortex response to this heating profile included the generation of midlevel radial inflow and a midlevel tangential wind jet. This vertical profile of heating, as with convection outside of TC environments, generated potential vorticity (PV) anomalies in the midlevels (Raymond and Jiang 1990; May et al. 1994; May and Holland 1999). These features are consistent with stratiform rainband characteristics found in some full-physics modeling studies (e.g., Franklin et al. 2006; Moon and Nolan 2015).

In an observational study using airborne Doppler radar, DH13 noted many of these same structures in the rainband complex stratiform sector in Hurricane Rita. These included the midlevel tangential wind jet and a robust inflow layer, in their case was clearly descending throughout the width of the rainband. The reflectivity signature suggested ongoing microphysical processes that supported a structure of diabatic heating and cooling, aligning well with the MN10 experiments.

While MN10's finding is in good agreement with the observational evidence presented in DH13, certain aspects of the stratiform rainband still deserves further exploration. For instance, the rainband heating used in MN10 was rotating about the vortex center, mimicking the diabatic forcing imposed by a moving spiral rainband. In addition, the stratiform heating profile used in MN10 is common among typical observed stratiform precipitation. However, whether this stratiform structure remains realistic in a gradient wind environment, such as at the stratiform rainband region of a hurricane, is open to question. MN10 also considered a stationary rainband with a mixed heating profile, but no significant results were discussed. Therefore, fundamental differences associated with quasi-stationary rainbands of stratiform heating still need further investigation.

This study aims at exploring these unaddressed questions by using Weather Research and Forecasting (WRF) Model idealized simulations to study the response of a dry, idealized hurricane-like vortex to the presence of stationary stratiform rainband heating. A brief overview of TC stratiform rainbands is first provided in section 2. The details of the WRF Model settings, experiment setup, and heating profiles used in this study are presented in section 3. In section 4, we revisit the vortex response when using the same stratiform profile as in MN10, but without rotation of the rainband. In section 5, we investigate the vortex response when using a modified stratiform heating profile, which is derived using the secondary circulation data presented in DH13. Section 6 further explores the idealized circulation response when moisture and conditional instability are present in the atmosphere. The conclusions of this study are provided in section 7.

2. Observations of TC stratiform rainbands

Figure 1a depicts the precipitation structure of an SBC when the larger storm is embedded in moderate or strong deep-layer environmental wind shear. The SBC tends to align with the wind shear vector such that the more active convective upwind end lies in the right-of-shear half, while a broad swath of predominantly stratiform precipitation lies in the left-of-the-shear half, resulting in a quasi-stationary asymmetry for times on the order of days (Corbosiero and Molinari 2002, 2003; Chen et al. 2006; Hence and Houze 2012; Didlake et al. 2018). Riemer (2016) theorized that this asymmetry of having new convection being triggered in the right-of-shear quadrants was due to the overlapping of anomalous low-level moisture and anomalous low-level positive vorticity due to distortion of the moisture envelope and vortex vertical structure by the environmental shear. As these convective cells travel from the upwind to the downwind portions of the rainband, they display the life cycle of convection, ending with decaying stage stratiform precipitation in the left-of-shear quadrants (DH13). The horizontally invariant nature and large spatial coverage of the downwind stratiform rainband marks its difference from the stratiform portions near upwind rainbands that have embedded convective cells (Barnes et al. 1983).

Early studies also noted the importance of the stratiform sector of spiral rainbands on the intensity and structural evolution of TCs. By using Doppler wind profiler and sounding observations, May et al. (1994) found that the rainband of Tropical Storm Flo had prominent features characteristic of stratiform precipitation, including a mesoscale updraft and downdraft above and below the melting level, maximum horizontal convergence at the melting level, and a midlevel jet. Using satellite and radiosonde observations, May and Holland (1999) found that mesoscale vertical transports in the stratiform sector of Flo had PV generation that was large enough to create the midlevel jet and impact the storm evolution and structure. Hence and Houze (2008) also found similar mesoscale vertical transports in Hurricane Katrina's left-of-shear portions of the rainband complex.

Using idealized simulations of TCs, Franklin et al. (2006) confirmed this close association between the midlevel jet and the stratiform portion of the rainband. By turning off

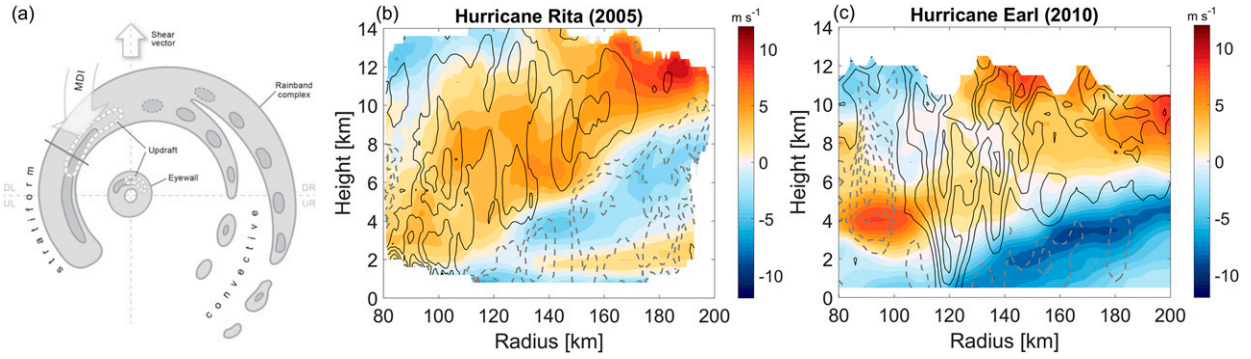

FIG. 1. (a) Plan view schematic of the rainband complex and eyewall (reflectivity contours of 20 and 35 dBZ) under the influence of environmental wind shear. The environmental wind shear vector points upward and defines the four storm quadrants. A mesoscale descending inflow (MDI) and an enhanced updraft (white dashes) both occur in the downshear-left (DL) quadrant within the stratiform sector of the rainband complex. From Didlake et al. (2018). (b) Cross section of the azimuthally averaged secondary circulation within the stratiform rainband sector of Hurricane Rita at 1642 UTC 21 Sep 2005. Updrafts (black contours) are shown at every 0.3 m s^{-1} from 0.3 to 1.5 m s^{-1}, and downdrafts (gray dashed contours) are shown at −0.1, −0.3, −0.6, and −0.9 m s^{-1}. From DH13. (c) As in (b), but for a cross section through the stratiform rainband of Hurricane Earl at 2038 UTC 29 Aug 2010. From Didlake et al. (2018).

cloud evaporation within the rainband, they further showed that the evaporative cooling associated with the stratiform precipitation is crucial in setting up the required buoyancy gradient for the PV generation and the existence of the midlevel tangential jet. This is consistent with the conclusions of DH13, who suggested that the diabatic cooling associated with sublimation, melting, and evaporation of Hurricane Rita's stratiform rainband were responsible for driving the observed secondary circulation within the rainband. As shown in Fig. 1b, within the stratiform rainband of Hurricane Rita, a robust layer of mesoscale inflow descended toward the boundary layer as it advanced radially inward [termed the mesoscale descending inflow (MDI)]. This negatively buoyant MDI brought in high angular momentum air from the storm environment and led to the emergence of a midlevel tangential jet. This process was also demonstrated by MN10 using idealized simulations. They found that the mesoscale overturning circulations and midlevel jet developed in response to stratiform heating project strongly onto the azimuthal mean of the storm. Their study showed the potential impact of a stratiform heating profile on the vortex-scale structure and that it differs from convective-type heating patterns. In a full-physics simulation, Moon and Nolan (2015) highlighted the structure of a downwind stratiform region of the rainband and also found descending inflow but at a lower altitude than that seen in observations.

Examining airborne Doppler radar observations of Hurricane Earl (2010), Didlake et al. (2018) again found a clear signature of an MDI and enhanced tangential jet in the downwind stratiform rainband (Fig. 1c). As shown by the black contour in Fig. 1c, just inward from the radii where the MDI reached the boundary layer, an intense low-level updraft occurred. This updraft was likely the result of low-level convergence induced by the advancing negatively buoyant MDI. Since these three features (i.e., MDI, enhanced tangential jet, and adjacent updraft) persistently occurred, accelerated the low-level tangential winds, and appeared just prior to the occurrence of secondary eyewall formation, Didlake et al. (2018) hypothesized that they sufficiently projected onto the azimuthal mean and led to the eventual development of Earl's secondary eyewall. The dynamics connecting these rainband features have yet to be thoroughly investigated using model simulations.

3. Methodology

a. Model and experiment setup

1) NUMERICAL MODEL

The Advanced Research version of the Weather Research and Forecasting (WRF-ARW) Model, version 3.9.1.1, is used to simulate the response of an idealized, dry hurricane-like vortex to the presence of a prescribed diabatic heating and cooling effects of a hurricane stratiform rainband. The model is configured to run at an f plane of 5×10^{-5} s^{-1} with triply nested domains with horizontal resolutions of 1, 3, and 9 km, and with 38 vertical levels up to 25-km altitude. The innermost, middle and outermost domains have 253 × 253, 139 × 139, and 301 × 301 grid points. Periodic boundary conditions are used at the lateral boundaries, and the outermost domain is designed to be large enough to prevent any boundary effect (if any) from reaching the middle and innermost domains within the analysis time window. The effect of rainband diabatic heating is represented

by a prescribed diabatic heating term Q ($\mathrm{K\,s^{-1}}$) added to the thermodynamic equation of the WRF Model (Skamarock et al. 2008) as

$$\frac{\partial \mu\theta}{\partial t} + \nabla \cdot (\mu \mathbf{u}\theta) = \mu F_\theta + \mu Q, \tag{1}$$

where θ is potential temperature, μ represents the mass per unit area, u is the three-dimensional wind vector, and F_θ is the model forcing from microphysics. To isolate the storm-scale response to the added diabatic forcing, all parameterization schemes, including microphysics, cumulus, and boundary schemes, are turned off. Without boundary layer friction, the lower boundary is a free-slip boundary condition. Therefore, the microphysics forcing term μF_θ in Eq. (1) is zero. Sensible heating and moisture fluxes at the lower boundary are also turned off.

2) Basic-state vortex

To compare our results with MN10's findings, the basic-state vortex used in the simulations is the same modified Rankine (MR) vortex wind profile as in MN10. The MR vortex is defined as

$$v(r,z) = \begin{cases} v_{\max}(z)\left[\dfrac{r}{\mathrm{RMW}(z)}\right], & r \le \mathrm{RMW}(z) \\ v_{\max}(z)\left[\dfrac{\mathrm{RMW}(z)}{r}\right]^a, & r > \mathrm{RMW}(z) \end{cases}, \tag{2}$$

where r is radius, z is altitude, $v_{\max}(z)$ and $\mathrm{RMW}(z)$ are the magnitude and radius of the maximum tangential wind, and the parameter a (taken as 0.5) controls the decay of the wind magnitude outside of RMW. Both $v_{\max}(z)$ and $\mathrm{RMW}(z)$ are derived by following the procedure described in the appendix of MN10. The thermodynamic fields that hold the vortex wind profile are then constructed using the iterative procedure of the built-in WRF initialization module for idealized hurricane simulations together with the Jordan (1958) mean hurricane sounding as the environmental temperature profile. With this vortex, we observed some weak gravity waves and vortex–Rossby waves radiating outward from the inner core of the vortex because of weak hydrostatic adjustment at the beginning. To prevent the interaction between this wave activity and the prescribed diabatic forcing, a 24-h spinup period is performed to allow the waves to decay or propagate out of the region where diabatic forcing is added. During the spinup period, the intensity of the vortex slightly weakens (surface maximum wind decreases from 43 to 40 $\mathrm{m\,s^{-1}}$) because of the presence of a sponge layer at the top of the domain (between z = 20 and 25 km). The storm structure remained unchanged. Sensitivity tests confirm that these small intensity changes do not impact the response induced by the rainband. Figures 2a and 2b show the profiles of the tangential wind and the potential temperature anomaly after the spinup period. After this spinup period, two 24-h-long experiments are conducted: one with the prescribed diabatic heating and the other without (control experiment). Following Kwon and Frank (2005), the response induced by the diabatic forcing is computed by subtracting the model fields of the two experiments. To compare with the results of MN10, all of the analyses of the response are evaluated at hour 18 after the spinup period, unless otherwise specified.

b. Design of diabatic heat source

1) Stratiform heating profile in MN10

We reexamine the storm-scale wind field response using the stratiform rainband heating profile in MN10. The radial and vertical structure of MN10's stratiform rainband is computed as

$$Q_{\mathrm{MN10}}(r,\lambda,z) = \begin{cases} 0, & \text{for} \quad z \le z_{bs} - \sigma_{zs} \\ Q_{\max} \exp\left[-\left(\dfrac{r - r_{bs}}{\sigma_{rs}}\right)^2 - \left(\dfrac{\lambda + \pi/4}{\pi/4}\right)^8\right] \sin\left(\dfrac{z - z_{bs}}{\sigma_{zs}}\pi\right), & \text{for} \quad z_{bs} - \sigma_{zs} < z < z_{bs} + \sigma_{zs} \\ 0, & \text{for} \quad z \ge z_{bs} + \sigma_{zs} \end{cases}, \tag{3}$$

where λ is azimuthal angle; $r_{bs}(\lambda, z)$ is the radial center location of the stratiform heating; z_{bs} is the vertical center location of the stratiform heating, which is also the level where transition from cooling to heating occurs (and therefore is of zero heating at z_{bs}); and σ_{rs} and σ_{zs} are the half-wavelengths that control the radial and vertical extents of the heating profile, respectively. The heating magnitude is controlled by $Q_{\max}$, which is taken to be 4.24 $\mathrm{K\,h^{-1}}$. Note that $r_{bs}(\lambda, z)$ is a function of height and azimuth and is designed to mimic the spiral structure and outward tilt of a tropical cyclone rainband. Following MN10's definition, $r_{bs}(\lambda, z)$

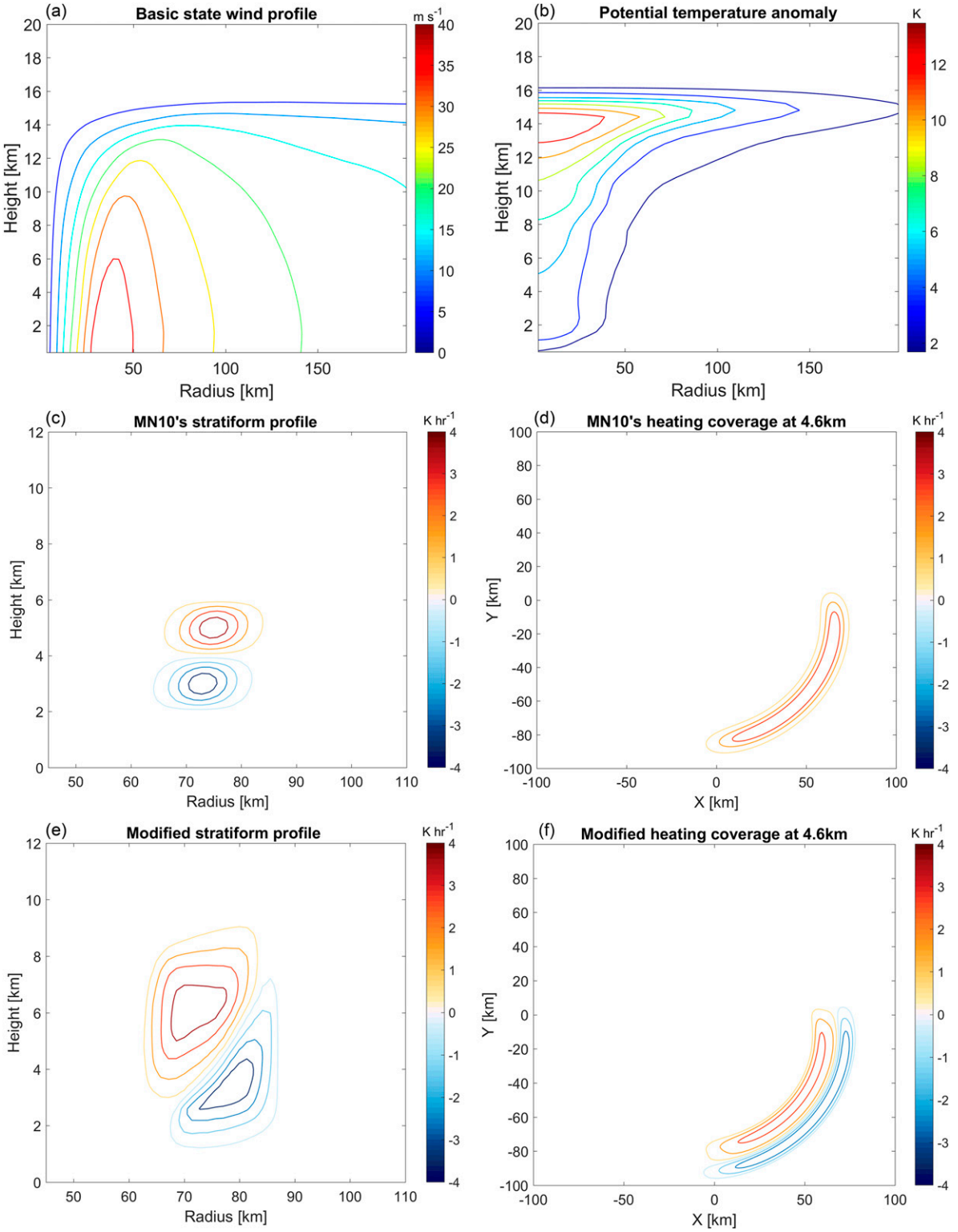

FIG. 2. Vertical and radial distributions of (a) tangential wind and (b) potential temperature anomaly of the basic-state vortex after the 24-h spinup period, contoured every 5 m s^{-1} and 1.69 K, respectively. (c) A cross section through the middle portion of MN10's stratiform rainband diabatic heating and (d) a plan view at $z = 4.6$ km . (e),(f) As in (c) and (d), but for the modified stratiform profile. Contour spacings are 1 K h^{-1} in (c) and (e) and 0.5 K h^{-1} in (d) and (f).

is given by $r_{bs}(\lambda, z) = r_{bsfc}(\lambda) + z$, where $r_{bsfc}(\lambda) = 60 - 10[\lambda/(\pi/4)]$ (km). This definition of $r_{bsfc}(\lambda)$ gives a spiral structure of the rainband that linearly varies from 60 km at the downwind end ($\lambda = 0$) to 80 km at the upwind end ($\lambda = -\pi/2$). The parameters z_{bs}, σ_{rs}, and σ_{zs} are taken to be 4, 6, and 2 km, respectively. The radial–height structure of MN10's stratiform profile at the middle of the rainband (i.e., $\lambda = -\pi/4$) is shown in Fig. 2c.

Note that the azimuthal coverage of the rainband heating in Eq. (3) is controlled by a stationary envelope, $\exp\{-[(\lambda + \pi/4)/(\pi/4)]^8\}$, which confines the rainband in the lower-right quadrant of the storm, as shown in Fig. 2d. This is different from MN10, whose rainband heating rotates at a constant rate of 70% of the tangential wind at the rainband region. Observational studies (Willoughby et al. 1984; Hence and Houze 2012) show that the stratiform sector of a rainband complex does not generally rotate at this rate, but rather remains quasi stationary and aligns with the environmental wind shear. While MN10 intensively studied the storm-scale wind field response with convective and stratiform rainbands that rotate with the tangential wind, rainbands that exhibit a stationary nature have not been fully explored. Therefore, in this study our stratiform rainband heating is designed to be stationary in the lower-right quadrant of the storm. Because of the presence of the stationary rainband forcing, we do observe some weak wobbling motion of the TC vortex, with a scale smaller than 1 km. Such small-scale wobbling of the storm center does not impact the evolution and analysis of the response. Therefore, in all the WRF simulations the rainband forcing is fixed in Cartesian space relative to the domain center, unless otherwise specified.

2) A MODIFIED STRATIFORM DIABATIC HEATING PROFILE BASED ON DH13

The MN10 idealized structure captures the basic heating profile of convection-driven stratiform precipitation, but its exact structure in a tropical cyclone may not be realistically represented by this idealized structure. We therefore design a modified structure that better matches the observed structures of a tropical cyclone rainband complex.

Our modified stratiform heating profile is based on the secondary circulation in the stratiform rainband of Hurricane Rita documented by DH13. DH13 found a seemingly closed secondary circulation that consists of a clear MDI and a rising outflow above and inward of it. We use the Sawyer–Eliassen equation (Eliassen 1951) to reconstruct the stratiform heating and cooling structure based on the azimuthally averaged secondary circulation shown in Fig. 1b. The details of the reconstruction process are presented in the appendix.

Based on the reconstructed diabatic heating and cooling derived from observational data, we designed the modified stratiform rainband heating and cooling profile shown in Figs. 2e and 2f. The radial coverage of the modified profile is confined to a radial range similar to MN10's stratiform profile, while the maximum heating rate and azimuthal coverage were kept the same. The modified profile captures the diagonal structure of the diabatic heating and cooling (as shown in Fig A1), with the low-level cooling located slightly radially outward from the upper-level heating. The altitude of the maximum heating is at 6 km, which is slightly higher than that of the stratiform profile in MN10, while the maximum cooling is at similar altitude. Given these differences, the modified profile structure at 4.6-km altitude (Fig. 2f) appears in a dipole pattern rather than a singular band of heating.

4. MN10 stratiform profile

a. *Axisymmetric response*

MN10 found that once the vortex reaches a steady state, the wavenumber-0 response of the primary circulation is a large component of the full tangential wind response. Figure 3a shows the axisymmetric responses of the tangential wind field and the secondary circulation on the r–z plane at simulation hour 18. Consistent with MN10 (as shown in Fig. 3b), the WRF simulation shows a clear axisymmetric tangential wind enhancement in the midlevels, with a maximum at $z = 4$ km, where the lower-level cooling transitions to upper-level heating. The axisymmetric rainband heating occurs approximately at 70-km radius. On the outward side of the axisymmetric heating is a clear midlevel inflow, which is collocated with the tangential wind enhancement. Radially inward, there is a slight decrease in tangential wind in the midlevels, which collocates with weak outflow between $r = 45$ and 65 km. This couplet of midlevel inflow and outflow and the associated horizontal convergence are driven by the rising and sinking motions induced by the diabatic heating and cooling. Conservation of angular momentum then results in the corresponding changes in the tangential wind. Both above and below the midlevel responses, vertical motion subsides and the flow diverges in weaker inflow–outflow couplets. This couplet, along with the corresponding changes in tangential wind, has an opposite configuration than that in the midlevels. While small differences do occur between the two axisymmetric responses in Fig. 3, the overall patterns are in good agreement.

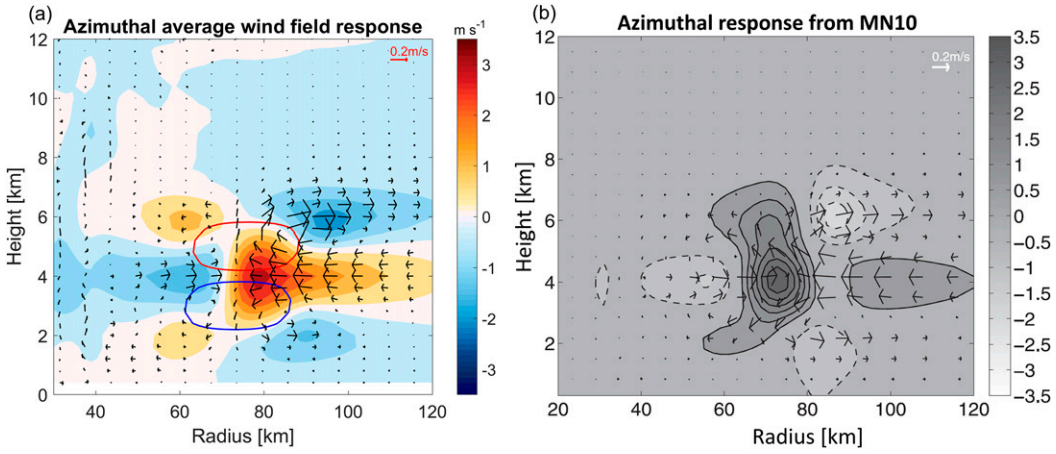

FIG. 3. (a) Azimuthally averaged wind field response using MN10's stratiform profile for the WRF simulation. Tangential velocity contours at intervals of 0.5 m s^{-1} are overlaid by the radial–vertical velocity vectors. Diabatic heating (cooling) of 0.15 (−0.15) K h^{-1} are highlighted by the solid red (blue) contour. (b) As in (a), but for MN10's simulation. From MN10. Solid (dashed) contours represent positive (negative) values.

b. *Plan view and cross-section analysis*

Figure 4 shows the individual plan views at different altitudes for the WRF and MN10 simulations. For the WRF simulation, we present both the full wind response (Figs. 4a–c) and the sum of responses for azimuthal wavenumbers 0–4 (Figs. 4d–f) in order to easily compare to the wavenumber-0–4 response from MN10 (Figs. 4g–i). At the midlevel (z = 3.6 km; Figs. 4b,e,h), the rainband regions (lower-right quadrant) for both simulations are dominated by sinking motion, while at the upper level (z = 6 km; Figs. 4a,d,g) rising motion is dominant. Some differences do occur at these two levels. For instance, a moderate downdraft not seen in MN10 occurs radially inward of the rainband heating at the upper level, while at the midlevel, a widespread but weak updraft is present in MN10's simulation. Otherwise, the responses at the middle and upper levels are generally in good agreement between the two experiments.

More noticeable differences can be found at the lower level of z = 2 km. As shown in Fig. 4f, the WRF simulation produces a band of downward motion along the spiral rainband arc, which is caused by the diabatic cooling below z = 4 km. Along the inner edge of this downdraft is a prominent band of low-level updraft. Both the updraft and downdraft appear to be stronger in the WRF full response (Fig. 4c). In MN10's simulation (Fig. 4i), this low-level band of upward motion is mostly absent, while the outer downdraft near the region of rainband cooling is also considerably weaker. As we will show in the next section, the main reason for these discrepancies in low-level vertical motion is the difference in rotation rates of the rainband heating.

Focusing on the WRF full wind field response, we look at cross sections slicing through the upwind, middle, and downwind portions of the rainband heating region, as shown in Fig. 5. For the tangential wind response, a uniform enhancement of tangential wind occurs across all three cross sections at about the same radial locations with similar magnitudes. The responses in the secondary circulation, on the other hand, have some variations across the rainband. The upwind portion shows the weakest response as this is the first region where the primary circulation enters the rainband and becomes modified by the heating structure. In the middle portion, the sinking motion associated with the midlevel inflow becomes significantly stronger, extending all the way to the lowest model level near r = 60 km. Consistent with Fig. 4c, radially inward between r = 40 and 60 km lies the low-level updraft, which extends vertically upward to z = 4 km and then becomes part of the midlevel outflow at the inward side of the rainband heating. Going farther downwind (Fig. 5d), the midlevel descending inflow gets even stronger and shifts inward, following the spiral structure of stratiform rainband.

Figure 4a shows that extending downwind of the rainband heating region, vertical motion responses occur along an inward spiral (highlighted by the gray shading). These wave responses also exist in the filtered response (Figs. 4d–f), which appear to be stronger than the Three-Dimensional Vortex Perturbation Analysis and Simulation (3DVPAS) simulation from MN10 (Figs. 4g–i). In the inner-core region, the WRF simulations also show inner-core wave modes, which appear to be in similar magnitude, but with different orientations from MN10's simulations. These differences are due

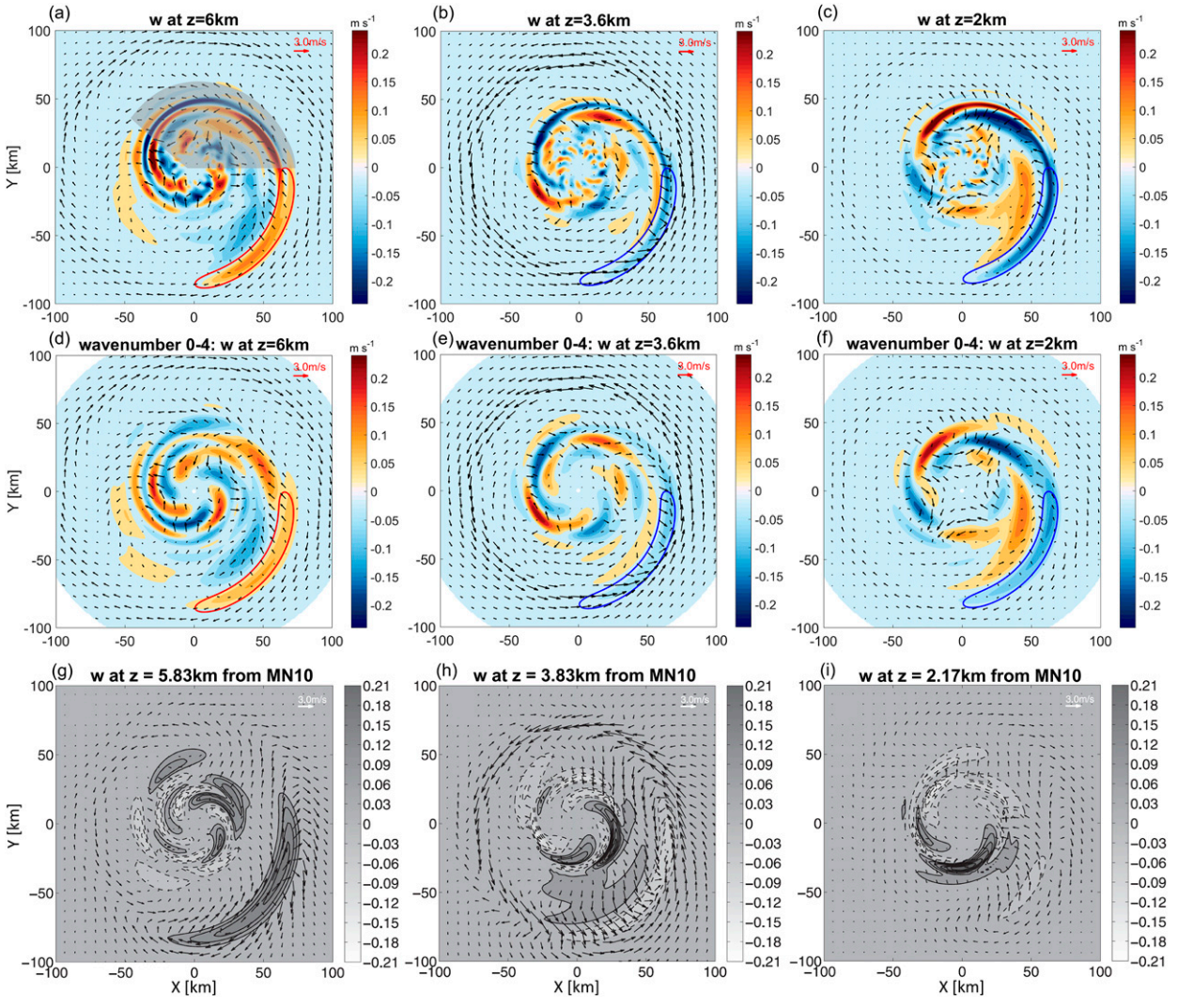

FIG. 4. Plan view of full responses in vertical velocity (shading) and horizontal wind field (vectors) responses at (a) 6-, (b) 3.6-, and (c) 2-km altitudes from MN10's stratiform heating using the WRF simulations. Solid contours of diabatic forcing with magnitude of 1 K h^{-1} (heating in red and cooling in blue) at 5.6, 3.6 and 2.4 km are added, respectively, to indicate the rainband location. (d)–(f) As in (a)–(c), but for responses summing from azimuthal wavenumbers 0 to 4. (g)–(i) As in (d)–(f), but from MN10's simulation at slightly different altitudes. Contours are at 0.03 m s^{-1} intervals.

mostly to the difference in rainband rotation rates between the two studies and the nonlinearity of the WRF Model. However, since there is no moisture and microphysics in the current experiment setting, it is difficult to quantify the actual impacts of these wave modes and their interaction with the rainband on the storm evolution. Thus, for the remainder of this study, we focus our analyses on the vortex responses within and surrounding the rainband region. Also, given the similarity between the WRF full (all wavenumbers) and filtered (sum of azimuthal wavenumbers 0–4) wind field responses, in the rest of the analysis we focus only on the full wind field responses, unless otherwise specified.

c. *Omega equation analysis*

Using MN10's stratiform profile, the midlevel descending inflow in our WRF simulation is consistent with both MN10's result and stratiform rainband observations (DH13; Didlake et al. 2018). Additionally, a low-level updraft is found on the radially inward side of the rainband. Didlake et al. (2018) found a similar low-level updraft in Hurricane Earl and hypothesized that this updraft occurred in response to the negatively buoyant MDI reaching the high–equivalent potential temperature (θ_e) boundary layer. This persistent low-level updraft likely played an important role forming the eventual secondary eyewall. In this section, we aim to

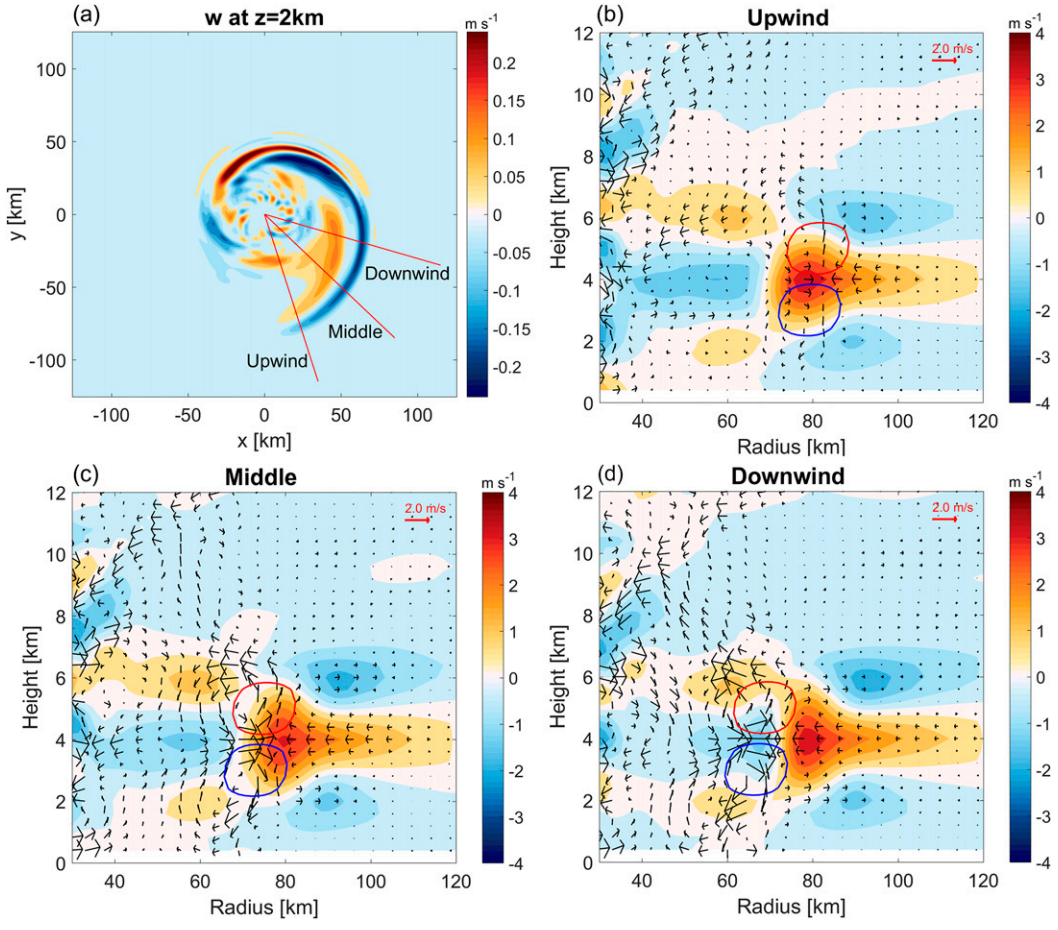

FIG. 5. (a) Plan view of vertical velocity at 2.2-km altitude from MN10's stratiform heating using the WRF simulation. Red lines mark the cross sections shown in the other panels. (b) Tangential wind (shading) and second circulation (vectors) responses from the WRF simulation in the upwind cross section in (a). (c) As in (b), but for the middle cross section. (d) As in (b), but for the downwind cross section. Diabatic heating (cooling) of 1 (−1) K h^{-1} are highlighted in solid red (blue) contours.

further explore the physical mechanism that generates this low-level updraft.

We employ the generalized omega equation derived by Krishnamurti (1968) based on a balanced assumption [Eq. (16) of Krishnamurti 1968; Eq. (23) of Zhang et al. 2000]. Similar to the quasigeostrophic (QG) omega equation, the generalized omega equation is a diagnostic equation for vertical motion. The generalized omega equation assumes hydrostatic balance and neglects the time derivative of divergence and advection by the divergent component of the wind field, while it includes the curvature effect of the flow, and therefore is applicable to flow regimes with relatively large Rossby number (Ro ~ 1). Neglecting the effects of differential deformation and differential divergence (small compared to other terms) and assuming a constant f plane, the generalized omega equation takes the following form:

$$\nabla_h^2(\sigma^2\omega) + f^2\frac{\partial^2\omega}{\partial p^2} - f\frac{\partial}{\partial p}\left(\omega\frac{\partial}{\partial p}\nabla_h^2\psi\right) - f\frac{\partial}{\partial p}\left(\nabla_h\omega\cdot\nabla_h\frac{\partial\psi}{\partial p}\right) = \frac{R}{c_p p}\nabla_h^2 H + f\frac{\partial}{\partial p}(\mathbf{u}_h\cdot\nabla_h\zeta) + \frac{RT}{p\theta}\nabla_h^2(\mathbf{u}_h\cdot\nabla_h\theta)\,, \qquad (4)$$

where $\nabla_h = \partial_x\mathbf{i} + \partial_y\mathbf{j}$ and $\nabla_h^2 = \partial_x^2 + \partial_y^2$ are the horizontal gradient and Laplacian operators, respectively; p, T, and θ are pressure, temperature, and potential temperature, respectively; $\omega = dp/dt$ is the pressure velocity; f is the Coriolis parameter; R and c_p are the ideal gas constant and specific heat capacity at constant pressure; ψ is the

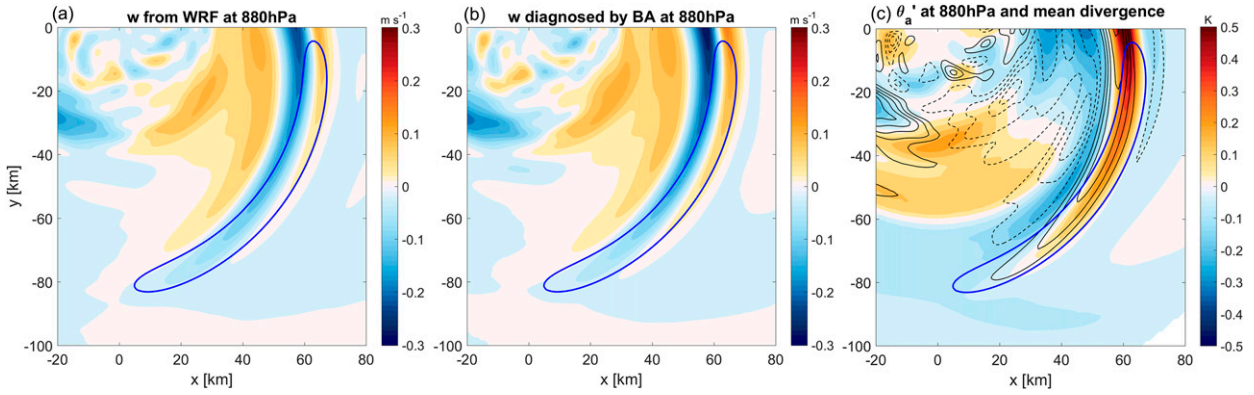

FIG. 6. (a) An 880-hPa-level (near $z = 1.15$ km) plan view of the vertical velocity response from MN10's stratiform heating in the WRF simulation in the lower-right quadrant. (b) Diagnosed vertical velocity from the buoyancy advection (BA) term in Eq. (5) corresponding to the vertical velocity field in (a). (c) The 880-hPa-level potential temperature anomalies and mean divergence between 880 hPa and the lowest pressure level using MN10's stratiform heating profile. Divergence contours are every 3×10^{-5} s^{-1}. Diabatic cooling of -0.5 K h^{-1} at 790 hPa is shown in solid blue contour.

streamfunction of the nondivergent horizontal wind; $\sigma^2 = -[RT/(p\theta)]\partial\theta/\partial p$ is the static stability parameter; H is the diabatic heating per unit mass of air; $\mathbf{u}_h$ is the horizontal wind vector; and ζ is relative vertical vorticity. Similar to the QG omega equation, the major forcings on the right-hand side of Eq. (4) are from diabatic heating (first term), differential vorticity advection (DVA; the second term) and buoyancy advection (BA; the third term). Equation (4) is solved numerically with initial guess $\omega_0 \equiv 0$ using the damped Jacobi method. The diagnosed ω is then converted into vertical velocity w. Figures 6a and 6b show a comparison of the vertical velocity from the WRF simulation and the diagnosed vertical velocity from the BA term at 880 hPa (about $z = 1.15$ km). It is clear that at this low level where the contribution of diabatic forcing is small, the BA term is the dominant, while DVA is at least two orders smaller (not shown).

Buoyancy advection can be understood by examining the potential temperature anomaly θ'_a, which is the deviation of potential temperature response θ' from its azimuthal average response (as a function of radius and height). The 880-hPa θ'_a (near $z = 1.15$ km, which is below the level of rainband cooling) is shown in Fig. 6c. Since tangential wind is the dominant component of the horizontal wind, the azimuthal advection of θ' (which is equal to the azimuthal advection of θ'_a) is the dominant component of the buoyancy advection. Thus, the distribution of θ'_a clearly displays the azimuthal gradient of θ' that causes buoyancy advection. Downwind and inward of the rainband cooling (as indicated by the blue contour in Fig. 6c), θ'_a shows a stationary negative anomaly, which is caused by the cold advection of the inward-advancing descending inflow. In contrast, the θ'_a is positive upwind and radially inward of the rainband heating, indicating that air coming from the upwind side is positively buoyant in a relative sense. As this upwind warm air advances into the rainband region, convergence occurs between these two air masses, as shown by the 880–1000-hPa layer-mean horizontal divergence in Fig. 6c. This results in a localized updraft on the inner edge of the rainband diabatic cooling. This mechanism shows that the θ' gradient and the resulting advection of θ' is essential to generate the enhanced low-level updraft.

d. *Pressure field analysis*

We next build on the dynamical analysis of the low-level updraft by examining the pressure responses associated with the stratiform heating. Figure 7a shows the cross section of pressure response along the downwind portion of the rainband. Below $z = 2$ km, the rainband cooling induces a high-pressure anomaly, while a predominant low-pressure anomaly is present between $z = 2$ and 6 km, where the transition between cooling and heating occurs. This is an expected pressure pattern of hydrostatic adjustment given diabatic cooling in the mid- to lower troposphere and has also been demonstrated in other rainband modeling studies (Wang 2009). Figure 7a also shows the low-level updraft of interest between 40- and 55-km radius. To see exactly how this pressure field response helps to maintain the low-level updraft, we first decompose the pressure response p' following Eq. (7.3) from Houze (2010):

$$\nabla^2 p' = \frac{\partial}{\partial z}(\rho_0 B) - \nabla \cdot \left(\rho_0 \mathbf{u} \cdot \nabla \mathbf{u} + \rho_0 \frac{v_0^2}{r}\hat{\mathbf{r}}\right) = F_B + F_D, \quad (5)$$

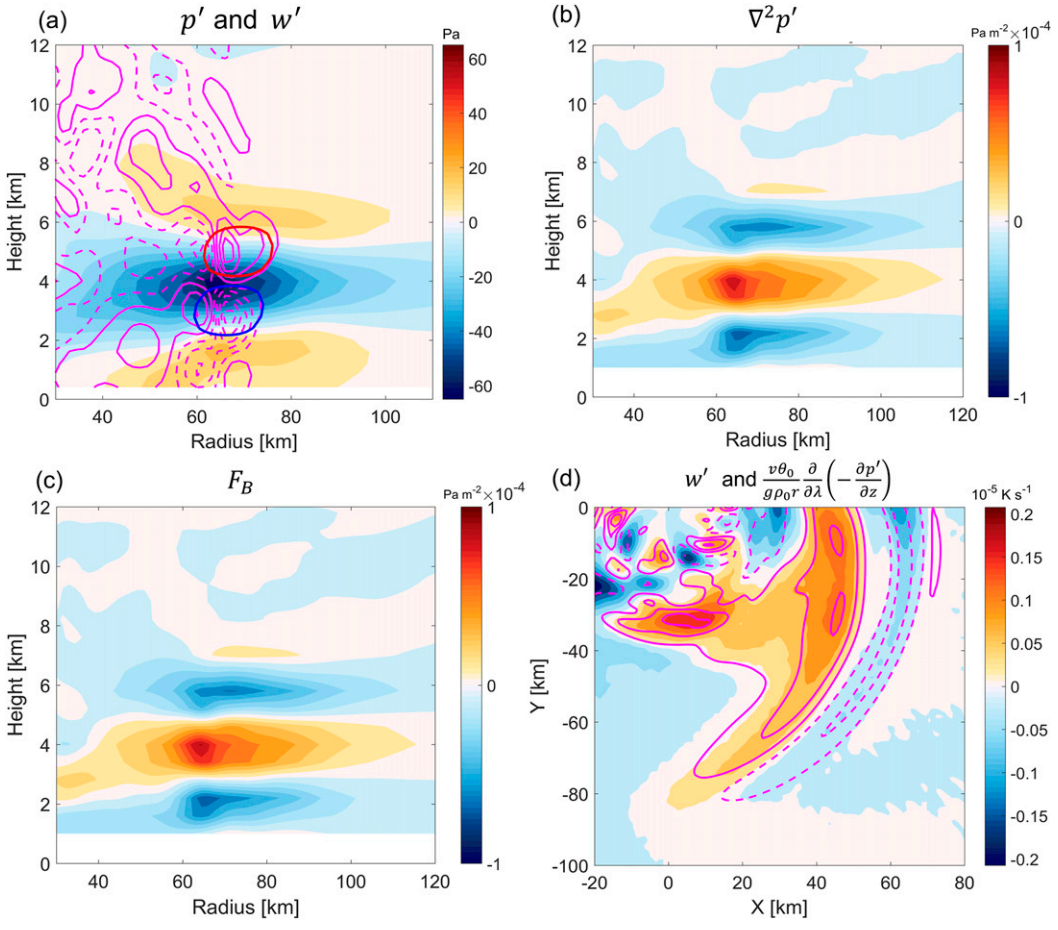

FIG. 7. (a) Cross section showing the responses in the pressure field (shading) and vertical velocity (magenta contours; negative values are dashed) at the downwind cross section in Fig. 5a. Vertical velocity is contoured at intervals of 0.082 m s^{-1}. Diabatic heating (cooling) values of 1 (-1) K h^{-1} are highlighted in red (blue) dashed contours. (b) The 3D Laplacian of the pressure response at the downwind cross section in Fig. 5a. (c) The buoyancy pressure forcing F_B at the downwind cross section in Fig. 5a. (d) Plan view of $[v\theta_0/(gr\rho_0)](\partial/\partial\lambda)(-\partial p'/\partial z)$ (shading) and vertical velocity response (magenta contours; negative values are dashed) at $z = 2$ km of the rainband quadrant. Vertical velocity is contoured at 0.05 m s^{-1}.

where $F_B = (\partial/\partial z)(\rho_0 B)$ is the buoyancy pressure forcing, $F_D = -\nabla \cdot [\rho_0 \mathbf{u} \cdot \nabla \mathbf{u} + \rho_0 (v_0^2/r)\hat{\mathbf{r}}]$ is the dynamic pressure forcing that accounts for the control experiment being in gradient wind balance, $B = -(\rho'/\rho_0)g$ is buoyancy with ρ' being the density response and ρ_0 the density field of the control experiment, $\mathbf{u}$ is the three-dimensional wind vector of the heating experiment, v_o is the tangential wind of the control experiment, and r and $\hat{\mathbf{r}}$ are radius and the unit vector in the radial direction. Figures 7b and 7c show the cross sections of $\nabla^2 p'$ and F_B along the downwind portion of the rainband. The pressure field response is largely due to buoyancy pressure forcing, while the dynamic pressure forcing is two orders of magnitude smaller (not shown). This buoyancy-driven nature suggests that the pressure response is the result of negatively buoyant air (induced by the rainband cooling) accumulating near the surface. A scale analysis (not shown) shows that the dominant component of $\nabla^2 p'$ is the vertical component. Thus, Eq. (5) can be approximated as $\partial^2 p'/\partial z^2 \approx \partial(\rho_0 B)/\partial z$. This indicates that the pressure and density responses are close to hydrostatic balance, which can be approximated as $(1/\rho_0)(\partial p'/\partial z) \approx -(\rho'/\rho_0)g \approx (\theta'/\theta_0)g$, where θ_0 is potential temperature of the control experiment (Markowski and Richardson 2010). On the other hand, because the dominant terms in Eq. (4) (i.e., $\nabla_h^2(\sigma^2\omega)$ on the left-hand side and $(RT/p\theta)\nabla_h^2(\mathbf{u} \cdot \nabla_h \theta)$ on the right-hand side) both contain the ∇_h^2 operator, the vertical motion and buoyancy advection fields share very similar structure. Hence, we have the following approximated relationship between w and the azimuthal gradient of vertical pressure gradient force:

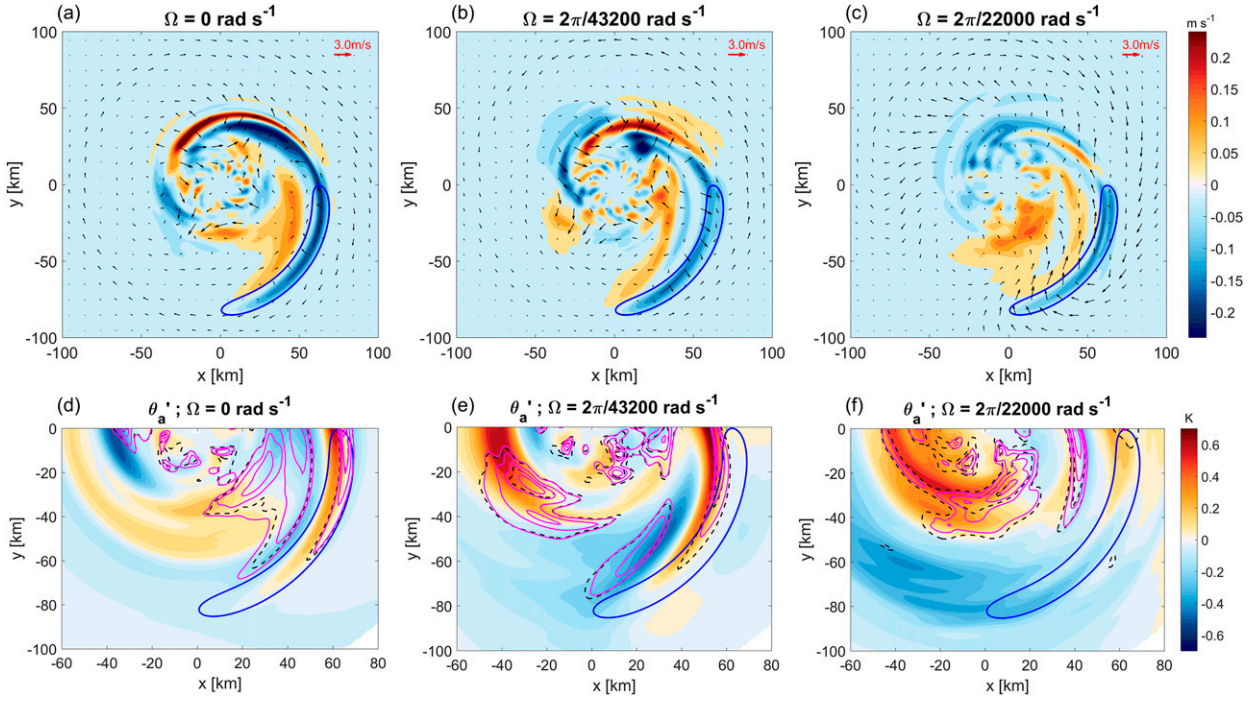

FIG. 8. Vertical velocity responses at $z = 2$ km using MN10's stratiform heating profile at different rainband rotation rates Ω: (a) no rainband rotation (Ω = 0), (b) $\Omega = 1.454 \times 10^{-4}$ rad s^{-1}, and (c) $\Omega = 2.856 \times 10^{-4}$ rad s^{-1}. Diabatic cooling of -1 K h^{-1} at 2.4 km is shown as a solid blue contour. (d) Anomalies of potential temperature response θ_a' (shading) at $z = 1$ km. Positive vertical velocity response w' (magenta contours) and buoyancy advection ($-\mathbf{u}_h \cdot \nabla_h \theta'$, black dashed contours) are contoured at 0.03 m s^{-1} and 1.2×10^{-5} K s^{-1}, respectively. (e) As in (d), but for $\Omega = 1.454 \times 10^{-4}$ rad s^{-1}. (f) As in (d), but for $\Omega = 2.856 \times 10^{-4}$ rad s^{-1}.

$$w \propto -\frac{v}{r}\frac{\partial \theta'}{\partial \lambda} \approx -\frac{v\theta_0}{gr\rho_0}\frac{\partial}{\partial \lambda}\left(\frac{\partial p'}{\partial z}\right), \tag{6}$$

where λ is the azimuthal angle. Figure 7d shows that the distribution of vertical velocity and $-[v\theta_0/(gr\rho_0)](\partial/\partial\lambda)(\partial p'/\partial z)$ correspond well. This indicates that as the air on the upwind side travels downwind, it experiences an enhancing vertical pressure gradient force [i.e., $(v/r)(\partial/\partial\lambda)(-\partial p'/\partial z) > 0$] associated with the cold and dense air accumulated at the downwind portion of the rainband, which provides the lifting force for the observed low-level updraft.

e. *Rotating rainband experiments*

The physical mechanism discussed in sections 4c and 4d suggests that the stationary nature of the rainband diabatic forcing is essential for generating the enhanced low-level updraft. To test this hypothesis, two more experiments are performed with the rainband heating structure rotating at an angular velocity of 1.454×10^{-4} and 2.856×10^{-4} rad s^{-1}, the latter of which is similar to the rotation rate used in MN10's simulation. Figure 8 shows a comparison of the vertical velocity and θ_a' at $z = 2$ km between the three experiments. All three experiments have positive vertical motion radially inward from the rainband region, with decreasing magnitude at faster rainband rotation rates. Also, the faster the rainband rotates, the more the negative θ_a' shifts toward the upwind side of the rainband, and the more widespread they become. Consequently, the azimuthal temperature gradient is much reduced and the resulting region of positive buoyancy advection (black dashed contours) becomes narrower and weaker, and so does the low-level updraft (solid magenta contours). These results demonstrate that the stationary nature of the rainband in the WRF simulations is the major cause of the differences in the low-level updraft response between the WRF simulation and MN10's findings.

We also note that with a rotation rate similar to MN10, the WRF Model still produced noticeable low-level upward motion radially inward of the rainband, (Fig. 8c), which is absent in the 3DVPAS simulation from MN10 (Fig. 4i). Additionally, the downdraft induced by the rainband diabatic cooling is also stronger compared to that in Fig. 4i. These weak vertical motions also exist in the WRF filtered response (wavenumbers 0–4, not shown), indicating that the differences are not caused by wave filtering. These differences may partly be due to the nonlinearity of the WRF Model, but the exact reason remains unclear. Also, both the orientation and structure of the inner-core wave modes vary across

the three experiments, which is likely caused by the nonlinear interaction between these wave modes and the induced circulation by the rainband heating.

5. Modified stratiform heating profile

a. Axisymmetric response

While the design of MN10's stratiform profile is typical among most stratiform clouds due to dying convection (Houze 1997), whether or not this heating–cooling structure would remain the same within a strong gradient wind environment, such as a TC rainband region, is open to question. Based on the secondary circulation observed in Hurricane Rita (2015), DH13 hypothesized a diagonal pattern of latent heating and cooling (see their Fig. 17b), which is confirmed in our reconstruction of heating structure based on the Sawyer–Eliassen equation (see appendix). This diagonal pattern of heating and cooling enhances the radial gradient of diabatic forcing, which may further enhance the secondary circulation (as indicated by the Sawyer–Eliassen equation; Eliassen 1951), as well as the midlevel descending inflow as seen in the previous simulations. Therefore, in this section we further explore how a TC-like vortex would respond to this modified stratiform heating structure.

Figure 9 shows the azimuthal average response in the tangential and secondary circulations with the modified stratiform heating–cooling profile. Overall, the azimuthal average response shares some similarities with the MN10 profile (Fig. 3a), but important differences do occur. At the midlevels near $z = 4$ km, we again see strong inflow and a weaker outflow on the two sides of the rainband heating, which converge near $r = 70$ km. Compared to the MN10 profile, these responses are deeper, with a larger portion of the midlevel inflow being directed downward toward the low levels and forming a clear descending inflow. This feature is in good agreement with the MDI observed in Hurricanes Rita (2005; DH13) and Earl (2010; Didlake et al. 2018). Following angular momentum conservation, a layer of tangential wind enhancement, which is noticeably deeper than that of MN10's stratiform rainband heating, is collocated with the simulated MDI. Owing to the noticeably stronger descent, the tangential wind jet also shows a descending pattern with its jet core located in the lower half of inflow layer.

b. Plan view and cross-section analysis

More differences with MN10 are revealed when examining plan views of different levels and cross sections. Figure 10 shows that the overall vertical velocity pattern near the rainband heating and cooling appears similar to that seen in the case of MN10 (Fig. 4). One exception is

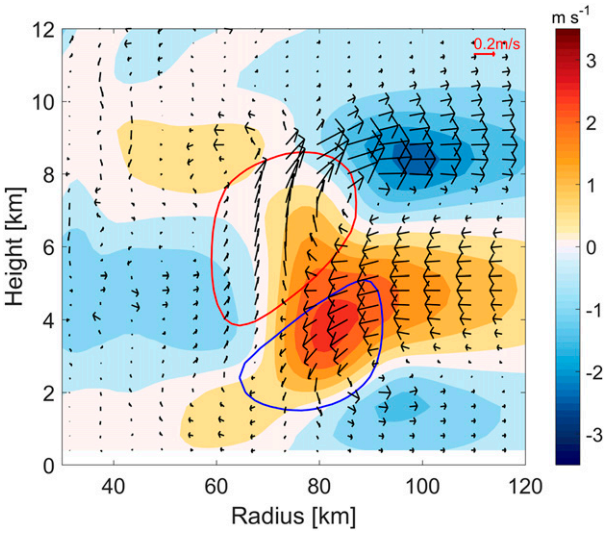

FIG. 9. Azimuthally averaged response of tangential wind (shading) and secondary circulation (vectors) from the WRF simulation using the modified stratiform heating profile. Diabatic heating (cooling) values of 0.15 (−0.15) K h^{-1} are highlighted by a solid red (blue) contour.

that the modified heating pattern produces stronger vertical velocities. In Fig. 11, the midlevel inflow across all three cross sections shows a very clear descending pattern near $r = 80$ km, as with the axisymmetric response. This pattern allows the accompanying high-angular-momentum air from larger radii to reach the surface more readily, resulting in enhanced tangential winds that skew toward the lowest levels. In the middle and downwind cross sections, a branch of midlevel rising outflow branch can also be seen around $z = 4$ to 6 km, as shown in Fig. 11d. Conserving its angular momentum, this rising outflow branch is associated with the upper-level anticyclonic circulation, which is also significantly stronger than that in MN10's stratiform profile, as shown in Fig. 5.

Inward of the descending inflow lies a low-level updraft similar to that from MN10's stratiform heating, but with a noticeably larger magnitude, especially in the middle portion (Fig. 11c). Also different from MN10's heating profile, this updraft band strongly curves inward, eventually separating from the midlevel rising outflow, as can be seen in Fig. 10c and Figs. 11c and 11d. This likely indicates that the two updrafts at low levels and at mid- to upper levels have different origins. Further investigation of the diagnostic omega equation terms [Eq. (4)] from the low-level updraft (not shown) showed that the BA term alone reproduced most of the low-level updraft, as in Fig. 6b. The associated θ' anomalies showed that negatively buoyant air from the modified stratiform cooling extended to smaller radii, causing a

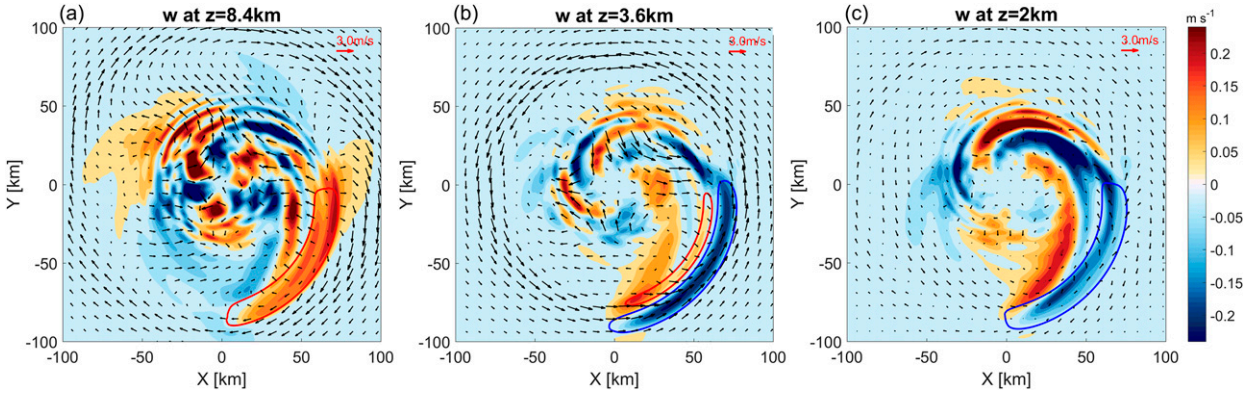

FIG. 10. Plan view of vertical velocity (shading) and horizontal wind field (vectors) responses at (a) 8.4-, (b) 3.6-, and (c) 2-km altitudes for the WRF simulations using the modified heating profile. Solid contours of diabatic forcing with a magnitude of 1 K h^{-1} (heating in red and cooling in blue) at 8, 3.6, and 2.4 km are added, respectively, to indicate the rainband location.

convergence zone between the warm and cold air masses and hence an updraft to spiral inward more strongly.

One should note that the current modified profile has slightly larger radial and vertical extent compared to the MN10's profile, and hence a larger total integrated absolute diabatic forcing. We have performed a parallel simulation of the modified heating structure but with a total integrated heating equal to that of the MN10

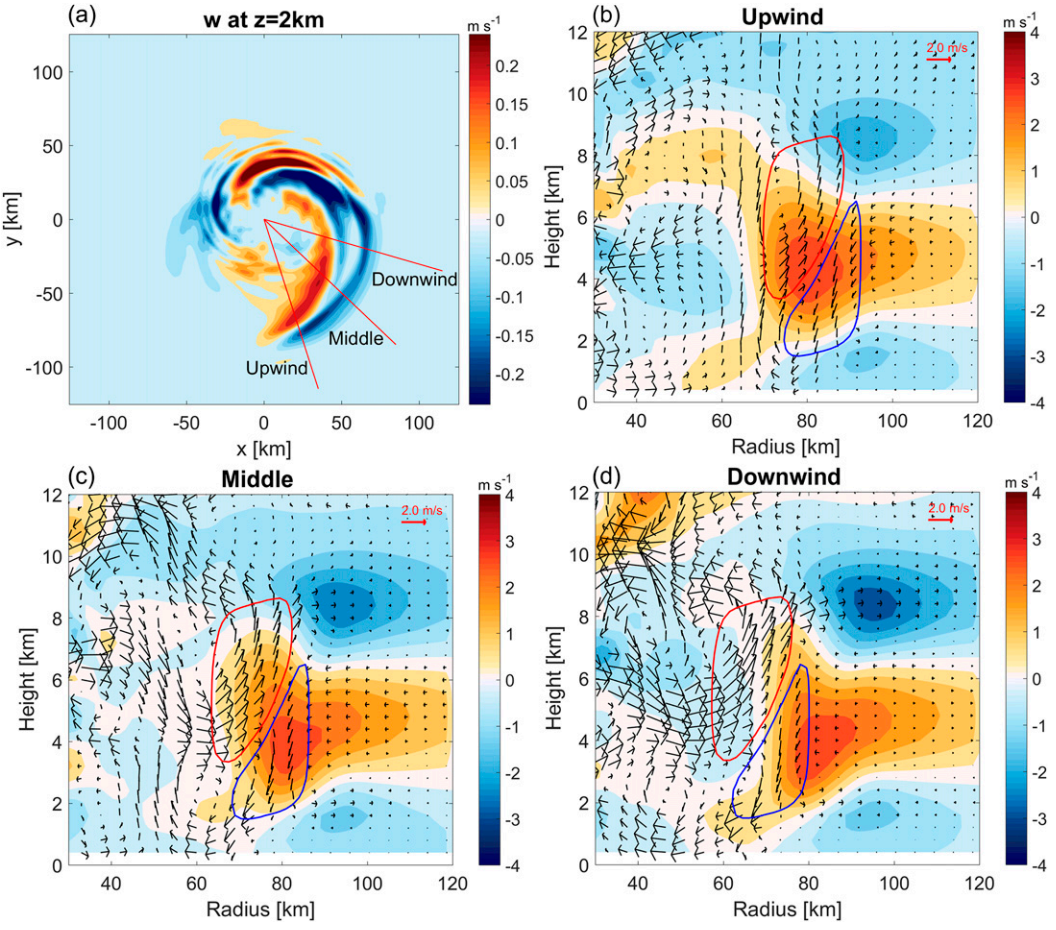

FIG. 11. As in Fig. 5, but for the modified heating profile.

heating profile. Our results show that while the magnitude of the circulation response varies with the integrated heating magnitude, the structure of the circulation response remains the same.

6. Buoyant updraft analysis

Thus far, we have analyzed the generation mechanism of the low-level updraft response to the idealized stratiform heating structures. One important aspect of interest is understanding how this low-level updraft impacts the evolution of the larger TC. The motivation for this interest is that the low-level updraft may be capable of triggering convectively buoyant updrafts that can further influence the intensity and structure of the TC, such as the updrafts found in Hurricane Earl (Fig. 1c). We found that the low-level updraft mostly does not overlap with the region of imposed diabatic heating and cooling. Given our current model setup with no moisture or microphysics, a rising air parcel in a stably stratified atmosphere will eventually become negatively buoyant. Thus, the potential evolution of the low-level updraft in a real atmosphere has not been fully explored. To answer this question, we conducted a new set of experiments that determines the convective buoyancy of air parcels being forced upward. To do this, we reinitialize the WRF Model with added moisture of various degrees of relative humidity (90%, 93%, and 95%) and with a microphysics parameterization [WRF single-moment 6-class microphysics scheme (WSM6)] turned on (in addition to the prescribed modified heating profile, as in Figs. 2e and 2f). As in the previous simulations, there is no boundary layer or cumulus parameterizations. The profiles of mean relative humidity averaged over an annulus covering the rainband region (40–80-km radius) are shown in Fig. 12. These modified profiles were based on the Jordan mean hurricane sounding. The amount of specific humidity added to the Jordan sounding at each level to achieve the desired relative humidity below 600 hPa is shown by the dashed lines in Fig. 12. Because of the added moisture, we did not perform a 24-h spinup in the following experiments; we verified that this change does not modify the overall dynamic response. The model is integrated for a short period of 6 h to collect statistics of the convectively buoyant updrafts (as defined below).

We define a parcel at a given grid point (x, y, z) as convectively buoyant if it meets the following criteria. First, the grid point must have a positive vertical velocity. Second, the associated vertical kinetic energy $(1/2)w^2$ must be greater than the convective inhibition (CIN) that it will experience. CIN is calculated as

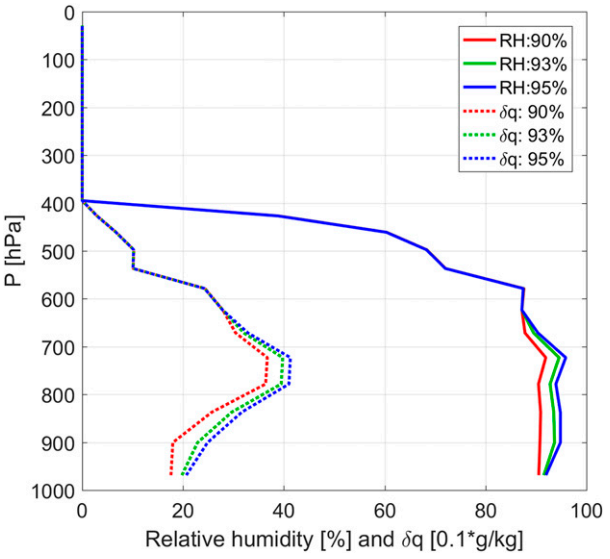

FIG. 12. Solid lines show the mean profiles of relative humidity for each moist sensitivity experiment, averaged over an annulus of 40–80-km radius, which covers the rainband region. Dashed lines show the specific humidity added to the Jordan mean hurricane sounding δq at each pressure level to initialize the experiments.

$$\mathrm{CIN} = -\int_{p_0}^{p_{\mathrm{LFC}}} R_{\mathrm{dry}}[T_{\mathrm{evn}}(p') - T_{\mathrm{parcel}}(p')]d\ln p', \qquad (7)$$

where p is pressure, p_0 is the initial level of the parcel under consideration, p_{LFC} is the level of free convection, R_{dry} is the gas constant for dry air, $T_{\mathrm{parcel}}(p)$ is the temperature the air parcel of interest would have if it is lifted upward from p_0 to p, and $T_{\mathrm{env}}(p)$ is the temperature profile of the atmospheric column at the same horizontal location as the air parcel. CIN and vertical kinetic energy are calculated for all grid points below 600-hPa height. If p_{LFC} for a given air parcel is higher than 400 hPa, the parcel is automatically flagged as nonconvective, since above this altitude the CIN is likely to be large enough to suppress the air parcel from being convectively buoyant. At any given time instant, if any grid point within a column is found to be convectively buoyant, we will count the entire column as a convectively buoyant column.

Figure 13 shows the frequency of convectively buoyant columns between simulation hours 2 and 6 for each humidity profile. All three experiments have a high frequency of buoyant columns at the locations of the low-level updraft. Expectedly, the higher relative humidity environments (Fig. 13c) were more likely to have convectively buoyant columns. The locations with larger frequencies lie entirely inward of the radii where upper-level heating (indicated by the black solid line) is located, showing that most of the induced buoyant updrafts are

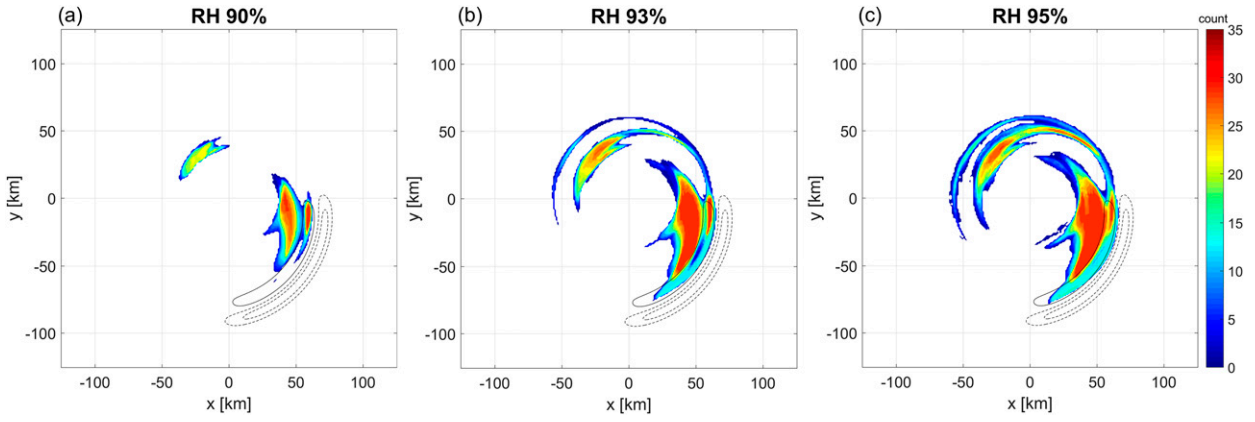

FIG. 13. Frequencies of buoyant convective updrafts occurring during simulation hours 2–6 using our modified heating profile with different relative humidity profiles: (a) 90%, (b) 93%, and (c) 95%. Contours of diabatic heating (solid) and cooling (dashed) at $z = 4$ km are shown as reference, with spacing of 2 K h^{-1}.

not directly associated with the imposed upper-level diabatic heating. Close inspection of individual updrafts (not shown) indicate that the low-level updraft identified in previous simulations becomes slightly stronger in magnitude because of diabatic heating release from the microphysics parameterization and that the location of the maximum updraft shifts slightly downwind and coincide with the regions of maximum frequency of buoyant columns, as in Fig. 13.

These results show that the low-level updrafts discussed in previous sections are capable of triggering convectively buoyant updrafts or new convective cells that may further impact the intensity and structure evolution of the TC. These convectively buoyant updrafts tend to be generated at the inward side of the stratiform rainband and may provide a plausible pathway for how a quasi-stationary stratiform rainband can produce sustained buoyant updrafts along its inner edge. In a related study, Chen (2018) also found that by continuously augmenting the low-level diabatic cooling at an annulus region outside of the primary eyewall, it is possible to synthetically produce a ring of persistent updrafts that eventually form an apparent secondary eyewall. Their findings align with previous observations (Didlake and Houze 2013a; Didlake et al. 2018) that indicate that diabatic cooling associated with the stratiform rainband is likely to play an important role in secondary eyewall formation. This same mechanism may also play a role in forming a wavenumber-1 asymmetry in a mature secondary eyewall through interaction with a stratiform rainband located just radially outward (Didlake et al. 2017). Based on our analysis, we believe that our findings may provide support to these studies from a dynamical standpoint.

7. Conclusions

In this study, we use idealized simulations of the Advanced Research version of the Weather Research and Forecasting Model to examine the one-way dynamic response of a dry hurricane-like vortex to stationary stratiform rainband diabatic forcing. Two stratiform rainband heating profiles have been investigated. One is the same stratiform heating profile used in MN10, which represents typical diabatic forcing in stratiform precipitation having heating above and cooling below the melting level. The second is a modified stratiform heating profile derived using the Sawyer–Eliassen equation and the observational data collected from Hurricane Rita (2005) as presented in DH13. In contrast to MN10's stratiform profile, the modified heating profile consists of a heating and cooling dipole in a diagonal pattern, creating an enhanced negative radial gradient of diabatic heating. Both stratiform heating profiles are stationary with respect to the vortex to mimic the diabatic forcing imposed by the stratiform portion of a quasi-stationary rainband complex.

Using MN10's stratiform profile, we reproduce secondary circulation and enhanced tangential wind responses that are largely consistent with the findings of MN10. When using the modified stratiform heating profile, both the midlevel inflow and enhancement of tangential flow are deeper in comparison. Owing to the larger radial gradient heating associated with the modified heating profile, most of the midlevel inflow descends toward the surface. This circulation pattern is similar in structure to the MDI observed in Hurricanes Earl (2010) and Rita (2005).

For both heating profiles, a low-level updraft response occurred radially inward of the MDI. A pressure field analysis shows that the low-level updrafts lie in a region

of enhanced upward-pointing pressure gradient force induced by buoyancy forcing. Using the generalized omega equation for balanced flow, we show that this low-level updraft is driven by the buoyancy advection term. This term indicates that the low-level updraft is caused by the azimuthal gradient of the near-surface temperature induced by the stratiform cooling and its advection by the vortex tangential flow. In experiments with the rainband rotating with the tangential flow rather than remaining stationary, the azimuthal temperature gradient was reduced and thus the low-level updraft magnitude was reduced. In experiments with moist thermodynamics and microphysics, the forced low-level updraft from the stationary rainband was sufficient for triggering persistent buoyant updrafts along the inner side of the rainband diabatic heating profile.

These experiments provide pertinent context for the features observed by Didlake et al. (2018) in the stratiform sector of Hurricane Earl (2010). Didlake et al. (2018) found a persistent deep updraft occurring at the terminus of the MDI. They proposed that the descent of the MDI disturbed the boundary layer and forced the adjacent deep updraft through buoyancy dynamics. Given the similarities with the simulated low-level updrafts, our experiments support their hypothesis, indicating that the MDI becomes a boundary layer cold pool that, through buoyancy advection by the tangential flow, triggers the adjacent buoyant updraft observed in the spiral rainband complex of Hurricane Earl.

The idealized experiments in this study provide insight to a potential mechanism for secondary eyewall formation in TCs. The persistent updraft in Earl accelerated the low-level tangential flow and was a precursor for the formation of an axisymmetric secondary tangential wind maximum and secondary eyewall. The stationary rainband complex from our experiments yield a persistent, spatially continuous, and deep updraft that spans the azimuthal extent of the stratiform rainband sector. Such an updraft would create a localized region of heating and enhanced low-level vorticity that would substantially project onto the azimuthal mean, as evidenced by the updraft and low-level tangential wind axisymmetric responses seen in Figs. 3a and 9. These responses could initiate secondary eyewall formation via several hypothesized axisymmetric dynamical mechanisms, such as upscale cascading of vorticity anomalies along a background radial vorticity gradient (Terwey and Montgomery 2008) or coupling with the boundary layer and inducing a positive feedback of enhancing convection (Wu et al. 2012; Huang et al. 2012, 2018; Abarca and Montgomery 2013, 2014; Kepert 2013, 2018; Zhang et al. 2017). Future work is still needed to investigate the axisymmetrization processes of stratiform rainband convection during secondary eyewall formation.

The current study presents a one-way response of a hurricane-like vortex to stratiform rainband heating without the presence of boundary layer and microphysics parameterizations. In addition, the diabatic forcing is prescribed and remains constant throughout the simulation, so any response of the circulation does not alter the structure of the diabatic forcing. More work is certainly needed to further investigate the response of the boundary layer circulation and how it interacts with the free atmosphere above. While we have attempted to anticipate the initiation of a convectively buoyant updraft from the forced low-level updraft, simulations with full microphysics and boundary layer parameterizations are needed to fully evaluate the proposed mechanism for convection initiation in a realistic TC environment. This subsequent impact on TC intensity and structural evolution would also need to be thoroughly examined.

Acknowledgments. We thank Fuqing Zhang, Paul Markowski, and David Nolan for their thoughtful comments on this study. We also thank the anonymous reviewers whose comments led to significant improvements in the manuscript. This research was supported by the National Science Foundation under Grant AGS-1810869.

APPENDIX

The Modified Stratiform Rainband Diabatic Forcing

In this appendix, we present the procedure of reconstructing the modified stratiform rainband heating from the secondary circulation observed in Hurricane Rita (2005) using the Sawyer–Eliassen equation (Eliassen 1951). The circulation data used is the azimuthally averaged radial and vertical velocity (u, w) fields (Fig. 1b) from leg 1 presented in DH13. A detailed description of the dataset can be found in section 2 of DH13. We used the Sawyer–Eliassen equation in z coordinates derived by Pendergrass and Willoughby (2009):

$$\frac{\partial b}{\partial z}\frac{\partial^2\psi}{\partial r^2} - 2\frac{\partial b}{\partial r}\frac{\partial^2\psi}{\partial z\partial r} + I^2\frac{\partial^2\psi}{\partial z^2} - \left(\frac{I^2}{H_\rho} - \frac{1}{R_\rho}\frac{\partial b}{\partial r} - \frac{3\xi S}{r} - N^2\frac{\partial\gamma}{\partial r}\right)\frac{\partial\psi}{\partial z} = r\rho\left[\frac{\partial Q}{\partial r} + \gamma\frac{\partial Q}{\partial z} - \frac{\partial(\xi M)}{\partial z}\right], \tag{A1}$$

where ψ is the mass streamfunction of the secondary circulation, b is buoyancy, I^2 is the inertial stability,

R_ρ and H_ρ are radial- and vertical-scale lengths of density ρ, γ is the ratio of radial pressure gradient force to gravitational acceleration, S is the vertical shear of the background wind v_0, $\xi = f + 2v_0/r$ is twice the absolute angular velocity, and M and Q are the momentum and heat sources, respectively.

The density field from the WRF Model after the 1-day spinup simulation is used to compute the mass flux $(\rho u, \rho w)$. To avoid the impact of frictional dissipation from boundary layer, all data below 2-km altitude are removed. To obtain the mass streamfunction ψ, the mass flux is decomposed into nondivergent $(\rho u_\psi, \rho w_\psi)$ and irrotational $(\rho u_\chi, \rho w_\chi)$ parts following Bijlsma et al. (1986):

$$
\begin{aligned}
&r\frac{\partial}{\partial r}\left(\frac{1}{r}\frac{\partial \psi}{\partial r}\right) + \frac{\partial^2 \psi}{\partial z^2} = -r\zeta \\
&\frac{1}{r}\frac{\partial}{\partial r}\left(r\frac{\partial \chi}{\partial r}\right) + \frac{\partial^2 \chi}{\partial z^2} = \delta \\
&(u_\psi, w_\psi)|_\partial + (u_\chi, w_\chi)|_\partial = (u, w)|_\partial; \quad \chi|_\partial = 0, \qquad \text{(A2)}
\end{aligned}
$$

where ψ is the mass streamfunction satisfying $\partial\psi/\partial z = -r\rho u_\psi$ and $\partial\psi/\partial r = r\rho w_\psi$; χ is velocity potential of $(\rho u_\chi, \rho w_\chi)$ satisfying $\partial\chi/\partial r = \rho u_\chi$ and $\partial\chi/\partial z = \rho w_\chi$; $\zeta = \partial\rho u/\partial z - \partial\rho w/\partial r$ and $\delta = (1/r)[\partial(r\rho u)/\partial r] + \partial\rho w/\partial z$ are the vorticity and divergence of $(\rho u, \rho w)$ on the r–z plane; and $|_\partial$ denotes evaluation at the boundary of the computation domain.

Results indicate that the irrotational part is small compared to the nondivergent part and the structure of ψ is insensitive to small variations of ρ. The ψ is then passed to Eq. (A1) to compute the total forcing term. To obtain the heating structure, the second and third terms in the right-hand side of Eq. (A1) are neglected, because the frictional effect is generally small in the computational domain and γ is small except near the radius of maximum wind (confirmed by a scale analysis not shown). The forcing $r\rho\partial Q/\partial r$ is then integrated radially inward from the outer boundary at $r = 190$ km to obtain the heating structure Q. Such a radial integration requires an initial vertical profile of heating $Q_0(z)$ at $r = 190$ km. Since in general the diabatic forcing is concentrated more at smaller radii in a tropical cyclone, this vertical heating profile $Q_0(z)$ at the outer boundary ($r = 190$ km) is assumed to be zero [i.e., $Q_0(z) = 0$].

Figure A1 shows the reconstructed diabatic forcing Q. Several features are prominent. It has a predominant heating region near 6-km altitude at the inner side, a low-level cooling region near and below 4-km altitude at the outer side, and the two of which form a clear diagonal pattern. We developed our modified stratiform heating profile (Fig. 2e) to capture the general pattern and prominent features of the reconstructed heating. Smoothed patterns were preferred to allow for a meaningful comparison with the MN10 heating profile. The exact structure for the modified heating is available in the online supplementary materials.

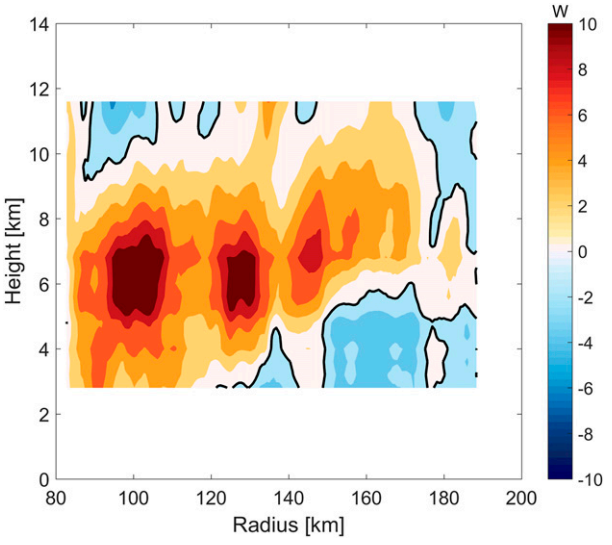

FIG. A1. Reconstructed diabatic heating using the Sawyer–Eliassen equation based on the observed secondary circulation within the stratiform rainband of Hurricane Rita (Fig. 1b). The zero contour is highlighted with a thick solid black line.

REFERENCES

Abarca, S. F., and M. T. Montgomery, 2013: Essential dynamics of secondary eyewall formation. *J. Atmos. Sci.*, **70**, 3216–3230, https://doi.org/10.1175/JAS-D-12-0318.1.

——, and ——, 2014: Departures from axisymmetric balance dynamics during secondary eyewall formation. *J. Atmos. Sci.*, **71**, 3723–3738, https://doi.org/10.1175/JAS-D-14-0018.1.

Barnes, G. M., D. P. Jorgensen, F. D. Marks Jr., and E. J. Zipser, 1983: Mesoscale and convective structure of a hurricane rainband. *J. Atmos. Sci.*, **40**, 2125–2137, https://doi.org/10.1175/1520-0469(1983)040<2125:MACSOA>2.0.CO;2.

Bijlsma, S. J., L. M. Hafkenscheid, and P. Lynch, 1986: Computation of the streamfunction and velocity potential and reconstruction of the wind fields. *Mon. Wea. Rev.*, **114**, 1547–1551, https://doi.org/10.1175/1520-0493(1986)114<1547:COTSAV>2.0.CO;2.

Chen, G., 2018: Secondary eyewall formation and concentric eyewall replacement in association with increased low-level inner-core diabatic cooling. *J. Atmos. Sci.*, **75**, 2659–2685, https://doi.org/10.1175/JAS-D-17-0207.1.

Chen, S. S., J. A. Knaff, and F. D. Marks Jr., 2006: Effects of vertical wind shear and storm motion on tropical cyclone rainfall asymmetries deduced from TRMM. *Mon. Wea. Rev.*, **134**, 3190–3208, https://doi.org/10.1175/MWR3245.1.

Corbosiero, K. L., and J. Molinari, 2002: The effects of vertical wind shear on the distribution of convection in tropical cyclones. *Mon. Wea. Rev.*, **130**, 2110–2123, https://doi.org/10.1175/1520-0493(2002)130<2110:TEOVWS>2.0.CO;2.

——, and ——, 2003: The relationship between storm motion, vertical wind shear, and convective asymmetries in tropical cyclones. *J. Atmos. Sci.*, **60**, 366–460, https://doi.org/10.1175/1520-0469(2003)060<0366:TRBSMV>2.0.CO;2.

Didlake, A. C., Jr., and R. A. Houze Jr., 2013a: Convective-scale variations in the inner-core rainbands of a tropical cyclone. *J. Atmos. Sci.*, **70**, 504–523, https://doi.org/10.1175/JAS-D-12-0134.1.

——, and ——, 2013b: Dynamics of the stratiform sector of a tropical cyclone rainband. *J. Atmos. Sci.*, **70**, 1891–1911, https://doi.org/10.1175/JAS-D-12-0245.1.

——, and M. R. Kumjian, 2017: Examining polarimetric radar observations of bulk microphysical structures and their relation to vortex kinematics in Hurricane Arthur (2014). *Mon. Wea. Rev.*, **145**, 4521–4541, https://doi.org/10.1175/MWR-D-17-0035.1.

——, G. M. Heymsfield, P. D. Reasor, and S. R. Guimond, 2017: Concentric eyewall asymmetries in Hurricane Gonzalo (2014) observed by airborne radar. *Mon. Wea. Rev.*, **145**, 729–749, https://doi.org/10.1175/MWR-D-16-0175.1.

——, P. D. Reasor, R. F. Rogers, and W.-C. Lee, 2018: Dynamics of the transition from spiral rainbands to a secondary eyewall in Hurricane Earl (2010). *J. Atmos. Sci.*, **75**, 2909–2929, https://doi.org/10.1175/JAS-D-17-0348.1.

Eliassen, A., 1951: Slow thermally or frictionally controlled meridional circulation in a circular vortex. *Astrophys. Nor.*, **5**, 19–60.

Franklin, C. N., G. J. Holland, and P. T. May, 2006: Mechanisms for the generation of mesoscale vorticity features in tropical cyclone rainbands. *Mon. Wea. Rev.*, **134**, 2649–2669, https://doi.org/10.1175/MWR3222.1.

Hence, D. A., and R. A. Houze Jr., 2008: Kinematic structure of convective-scale elements in the rainbands of Hurricanes Katrina and Rita (2005). *J. Geophys. Res.*, **113**, D15108, https://doi.org/10.1029/2007JD009429.

——, and ——, 2012: Vertical structure of tropical cyclones with concentric eyewalls as seen by the TRMM Precipitation Radar. *J. Atmos. Sci.*, **69**, 1021–1036, https://doi.org/10.1175/JAS-D-11-0119.1.

Houze, R. A., Jr., 1997: Stratiform precipitation in regions of convection: A meteorological paradox? *Bull. Amer. Meteor. Soc.*, **78**, 2179–2196, https://doi.org/10.1175/1520-0477(1997)078<2179:SPIROC>2.0.CO;2.

——, 2010: Clouds in tropical cyclones. *Mon. Wea. Rev.*, **138**, 293–344, https://doi.org/10.1175/2009MWR2989.1.

Huang, Y.-H., M. T. Montgomery, and C.-C. Wu, 2012: Concentric eyewall formation in Typhoon Sinlaku (2008). Part II: Axisymmetric dynamical processes. *J. Atmos. Sci.*, **69**, 662–674, https://doi.org/10.1175/JAS-D-11-0114.1.

——, C.-C. Wu, and M. T. Montgomery, 2018: Concentric eyewall formation in Typhoon Sinlaku (2008). Part III: Horizontal momentum budget analyses. *J. Atmos. Sci.*, **75**, 3541–3563, https://doi.org/10.1175/JAS-D-18-0037.1.

Jordan, C. L., 1958: Mean soundings for the West Indies area. *J. Meteor.*, **15**, 91–97, https://doi.org/10.1175/1520-0469(1958)015<0091:MSFTWI>2.0.CO;2.

Kepert, J. D., 2013: How does the boundary layer contribute to eyewall replacement cycles in axisymmetric tropical cyclones? *J. Atmos. Sci.*, **70**, 2808–2830, https://doi.org/10.1175/JAS-D-13-046.1.

——, 2018: The boundary layer dynamics of tropical cyclone rainbands. *J. Atmos. Sci.*, **75**, 3777–3795, https://doi.org/10.1175/JAS-D-18-0133.1.

Krishnamurti, T. N., 1968: A diagnostic balance model for studies of weather systems of low and high latitudes, Rossby number less than 1. *Mon. Wea. Rev.*, **96**, 197–207, https://doi.org/10.1175/1520-0493(1968)096<0197:ADBMFS>2.0.CO;2.

Kwon, Y. C., and W. M. Frank, 2005: Dynamic instabilities of simulated hurricane-like vortices and their impacts on the core structure of hurricanes. Part I: Dry experiments. *J. Atmos. Sci.*, **62**, 3955–3973, https://doi.org/10.1175/JAS3575.1.

Markowski, P. M., and Y. P. Richardson, 2010: *Mesoscale Meteorology in Midlatitudes*. Wiley-Blackwell, 424 pp.

May, P. T., 1996: The organization of convection in the rainbands of Tropical Cyclone Laurence. *Mon. Wea. Rev.*, **124**, 807–815, https://doi.org/10.1175/1520-0493(1996)124<0807:TOOCIT>2.0.CO;2.

——, and G. J. Holland, 1999: The role of potential vorticity generation in tropical cyclone rainbands. *J. Atmos. Sci.*, **56**, 1224–1228, https://doi.org/10.1175/1520-0469(1999)056<1224:TROPVG>2.0.CO;2.

——, ——, and W. L. Ecklund, 1994: Wind profiler observations of Tropical Storm Flo at Saipan. *Wea. Forecasting*, **9**, 410–426, https://doi.org/10.1175/1520-0434(1994)009<0410:WPOOTS>2.0.CO;2.

Moon, Y., and D. S. Nolan, 2010: The dynamic response of the hurricane wind field to spiral rainband heating. *J. Atmos. Sci.*, **67**, 1779–1805, https://doi.org/10.1175/2010JAS3171.1.

——, and ——, 2015: Spiral rainbands in a numerical simulation of Hurricane Bill (2009). Part I: Structures and comparisons to observations. *J. Atmos. Sci.*, **72**, 164–190, https://doi.org/10.1175/JAS-D-14-0058.1.

Pendergrass, A. G., and H. E. Willoughby, 2009: Diabatically induced secondary flows in tropical cyclones. Part I: Quasi-steady forcing. *Mon. Wea. Rev.*, **137**, 805–821, https://doi.org/10.1175/2008MWR2657.1.

Powell, M. D., 1990: Boundary layer structure and dynamics in outer hurricane rainbands. Part I: Mesoscale rainfall and kinematic structure. *Mon. Wea. Rev.*, **118**, 891–917, https://doi.org/10.1175/1520-0493(1990)118<0891:BLSADI>2.0.CO;2.

Raymond, D. J., and H. Jiang, 1990: A theory for long-lived mesoscale convective systems. *J. Atmos. Sci.*, **47**, 3067–3077, https://doi.org/10.1175/1520-0469(1990)047<3067:ATFLLM>2.0.CO;2.

Riemer, M., 2016: Meso-β-scale environment for the stationary band complex of vertically sheared tropical cyclones. *Quart. J. Roy. Meteor. Soc.*, **142**, 2442–2451, https://doi.org/10.1002/qj.2837.

Skamarock, W. C., and Coauthors, 2008: A description of the Advanced Research WRF version 3. NCAR Tech. Note NCAR/TN-475+STR, 113 pp., https://doi.org/10.5065/D68S4MVH.

Terwey, W. D., and M. T. Montgomery, 2008: Secondary eyewall formation in two idealized, full-physics modeled hurricanes. *J. Geophys. Res.*, **113**, D12112, https://doi.org/10.1029/2007JD008897.

Tyner, B., P. Zhu, J. A. Zhang, S. Gopalakrishnan, F. D. Marks Jr., and V. Tallapragada, 2018: A top-down pathway to secondary eyewall formation in simulated tropical cyclones. *J. Geophys. Res. Atmos.*, **123**, 174–197, https://doi.org/10.1002/2017JD027410.

Wang, Y., 2009: How do outer spiral rainbands affect tropical cyclone structure and intensity? *J. Atmos. Sci.*, **66**, 1250–1273, https://doi.org/10.1175/2008JAS2737.1.

Willoughby, H. E., F. D. Marks Jr., and R. J. Feinberg, 1984: Stationary and moving convective bands in hurricanes. *J. Atmos. Sci.*, **41**, 3189–3211, https://doi.org/10.1175/1520-0469(1984)041<3189:SAMCBI>2.0.CO;2.

Wu, C.-C., Y.-H. Huang, and G.-Y. Lien, 2012: Concentric eyewall formation in Typhoon Sinlaku (2008). Part I: Assimilation of T-PARC data based on the ensemble Kalman filter (EnKF). *Mon. Wea. Rev.*, **140**, 506–527, https://doi.org/10.1175/MWR-D-11-00057.1.

Zhang, F., S. E. Koch, C. A. Davis, and M. L. Kaplan, 2000: A survey of unbalanced flow diagnostics and their application. *Adv. Atmos. Sci.*, **17**, 165–183, https://doi.org/10.1007/s00376-000-0001-1.

——, D. Tao, Y. Q. Sun, and J. D. Kepert, 2017: Dynamics and predictability of secondary eyewall formation in sheared tropical cyclones. *J. Adv. Model. Earth Syst.*, **9**, 89–112, https://doi.org/10.1002/2016MS000729.